Article:

Herrera, Marcela, Reina, John H., D'Amico, Irene et al. (2023) Correlation-boosted quantum engine: A proof-of-principle demonstration. Physical Review Research. 043104. ISSN: 2643-1564

https://doi.org/10.1103/PhysRevResearch.5.043104

PHYSICAL REVIEW RESEARCH **5**, 043104 (2023)

Correlation-boosted quantum engine: A proof-of-principle demonstration

Marcela Herrera,[1,2,3,*] John H. Reina,[1,2,†] Irene D'Amico,[4,‡] and Roberto M. Serra[5,6,§]
[1]*Centre for Bioinformatics and Photonics-CIBioFi, Edificio E20 No. 1069, Universidad del Valle, 760032 Cali, Colombia*
[2]*Departamento de Física, Universidad del Valle, 760032 Cali, Colombia*
[3]*Facultad de Ciencias Básicas, Universidad Autónoma de Occidente, Cali, Colombia*
[4]*School of Physics, Engineering and Technology, University of York, York YO10 5DD, United Kingdom*
[5]*Centro de Ciências Naturais e Humanas, Universidade Federal do ABC, Avenida dos Estados 5001,*
09210-580 Santo André, São Paulo, Brazil
[6]*Department of Physics, Zhejiang Normal University, Jinhua 321004, China*

(Received 22 November 2022; revised 10 April 2023; accepted 1 June 2023; published 2 November 2023)

Employing currently available quantum technology, we design and implement a nonclassically correlated SWAP heat engine that allows to achieve an efficiency above the standard Carnot limit. Such an engine also boosts the amount of extractable work, in a wider parameter window, with respect to engine's cycle in the absence of initial quantum correlations in the working substance. The boosted efficiency arises from a trade-off between the entropy production and the consumption of quantum correlations during the full thermodynamic cycle. We derive a generalized second-law limit for the correlated cycle and implement a proof-of-principle demonstration of the engine efficiency enhancement by effectively tailoring the thermal engine on a cloud quantum processor.

DOI: 10.1103/PhysRevResearch.5.043104

I. INTRODUCTION

Recent years have witnessed the rise of quantum thermodynamics (QTD), which has rapidly become an arena to test and debate fundamental concepts such as the laws of thermodynamics and the related fluctuation theorems at the quantum scale [1–12]. In parallel, QTD is facilitating the extension of practical concepts such as heat and work towards the design [13–20] and, more recently, the implementation [2,21–27] of thermal machines based on a handful of quantum degrees of freedom. Particular attention is being given to the concept of entropy production for systems out of equilibrium [28–32] and to the—related—second law of thermodynamics [6,33,34], as well as to the role of quantum correlations in both fundamental concepts [35–39] and in the functioning of thermal devices [40–45]. Quantum features can be considered as extra resources. Squeezed states, for instance, can enhance the performance of a microscopic engine above its classical limits [17,46]. Coherence with a dynamical interference [47–49], quantum measurements [50–56], and quantum operations causal order [57–62] also play nontrivial roles in the performance of thermodynamic tasks [40,41].

Through the design and proof-of-principle implementation of a two-qubit thermal machine (on a quantum processor), here, we demonstrate that the use of quantum correlations as an extra resource can indeed lead to a generalized second law of thermodynamics encompassing regimes with efficiency larger than the standard Carnot limit. As an added bonus, quantum correlations increase the amount of extractable work, as well as extend the parameter region corresponding to useful work extraction for the proposed cycle.

This paper is organized as follows. Taking advantage of initial nonclassical correlations in a two-qubit working substance, in Sec. II, we design a correlated quantum heat-engine based on the concept of a partial SWAP operation. The engine's nonequilibrium-thermodynamics quantifiers are introduced and analytically computed in Sec. III. In Sec. IV, we introduce a quantum processor implementation of the quantum heat engine setup and experimentally demonstrate the performance enhancement of the proposed correlated SWAP heat engine. In Sec. V, we derive an analytical expression for the SWAP engine efficiency and provide a criterion for performance over the classical limit (above Carnot) to occur. In Sec. V A, we prove that such an engine can exceed the conventional classical limits, with an out-performance that is well described by an information-to-energy trade-off relation for the cycle efficiency, which can be seen as a quantum generalized efficiency limit for a two-stroke cycle in the presence of nonclassical correlations. In Secs. V B and V C, based on the ancilla-assisted two-point-measurement method developed in Ref. [26], we use a cloud quantum processor [63] to implement an experimental proof-of-principle of our design. Summary of results and concluding remarks are given in Sec. VI.

---

[*] amherrera@uao.edu.co
[†] john.reina@correounivalle.edu.co
[‡] irene.damico@york.ac.uk
[§] serra@ufabc.edu.br

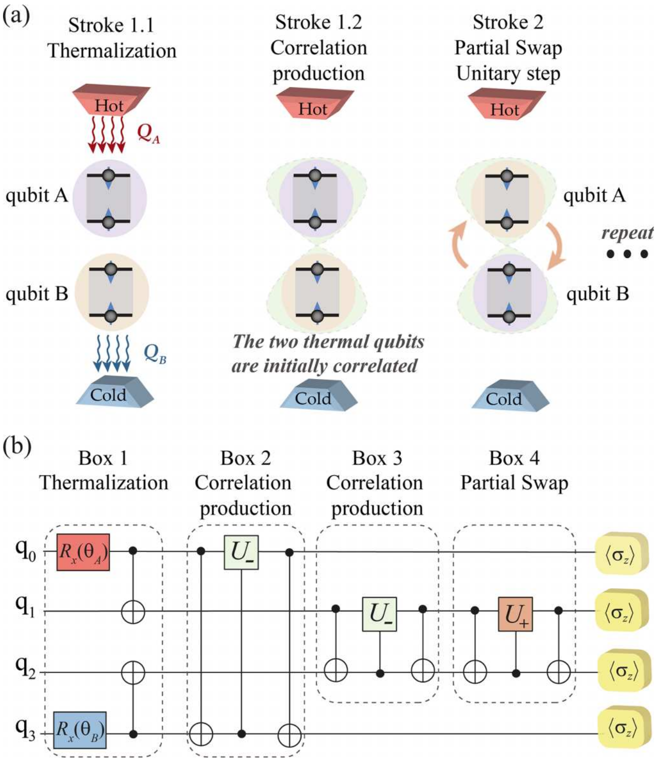

FIG. 1. (a) Thermodynamic cycle of a correlated SWAP quantum heat engine. The two-qubit (AB) system acts as the working substance. Q_A (Q_B) denotes the heat exchanged with the hot (cold) environment. (b) Quantum-circuit to test the correlated heat engine concept. The input to the circuit is the ground state $|0000\rangle$. The qubits q_0 and q_3 are employed as ancillae to prepare the engine in the initial thermal state $\rho_1^0 \otimes \rho_2^0 \equiv \tilde{\rho}_A^0 \otimes \tilde{\rho}_B^0$ (box 1); the rotation angles θ_i depend on α and the qubits effective temperature. The AB correlations are generated in boxes 2 and 3 via U_-, and the final partial SWAP implementation, via U_+, in box 4.

II. DESIGN AND FUNCTIONING OF A CORRELATED QUANTUM HEAT ENGINE

The quantum engine is composed by two qubits with energy gaps ε_A and ε_B. Each of them is initially coupled to an effective heat environment, as schematized in Fig. 1(a), stroke 1.1, which lead to the product of Gibbs states, $\tilde{\rho}_A^0 \otimes \tilde{\rho}_B^0$. After such a complete thermalization, the two qubits get correlated through stroke 1.2 [Fig. 1(a)] in a state given by

$$\rho_{AB}^0 = \rho_A^0 \otimes \rho_B^0 + \chi_{AB}, \tag{1}$$

where the reduced local state for each qubit $\rho_i^0 = \exp(-\beta_i \mathcal{H}_i)/\mathcal{Z}_i$ is a thermal equilibrium state at the inverse temperature $\beta_i = (k_B T_i)^{-1}$, $i = A, B$; $\mathcal{Z}_i = \mathrm{Tr}_i \exp(-\beta_i \mathcal{H}_i)$ is the corresponding partition function, and $\chi_{AB} = \alpha|01\rangle\langle 10| + \alpha^*|10\rangle\langle 01|$ gives the relevant correlation term, with $\mathrm{Tr}_i \chi_{AB} = 0$. Here, the states $|0\rangle$ and $|1\rangle$ denote the ground and excited eigenstates of the qubit Hamiltonian $\mathcal{H}_i = -\frac{1}{2}\varepsilon_i \sigma_Z^{(i)}$; the total two-qubit Hamiltonian $\mathcal{H}_{AB} = \mathcal{H}_A + \mathcal{H}_B$. Qubit A is assumed to be hotter than the qubit B, that is $\beta_A < \beta_B$. We remark that the correlation term χ_{AB} does not contribute to the energy of qubits A and B. The populations of states $\tilde{\rho}_A^0$ and $\tilde{\rho}_B^0$ are chosen in a way to obtain the desired correlated state in Eq. (1) (see Appendix A). The energy exchange between the two qubits is determined by means of a partial SWAP operation, as illustrated in Fig. 1(a), stroke 2, where work can be extracted from or performed on the quantum system. Physically, this can be implemented by an effective unitary Heisenberg exchange Hamiltonian evolution ($j = X, Y, Z$)

$$\mathcal{U}_t = \exp\left(\frac{-iJt}{2}\sum_j \sigma_j^{(A)} \otimes \sigma_j^{(B)}\right). \tag{2}$$

At $t = 0$, there is no interaction at all; a complete SWAP operation [64,65] takes place at $t = \pi/(2J)$.

Although the initial state Eq. (1) seems to be similar to the one considered in Ref. [41], we stress that the off-diagonal parameter has a different phase and the evolution is driven by a different Hamiltonian, which makes all the difference to exploit nonconvectional energy flows to thermal tasks. Moreover, the correlation parameter used in Ref. [41] would not allow for an advantage in the quantum heat engine here implemented.

Next, we consider a proof-of-principle implementation on a quantum processor. Figure 1(b) shows a quantum circuit that implements a partial SWAP engine in the presence of initial correlations. It is based on the use of the (controlled) gate $U_\pm(x) \equiv \mathbb{1}\sqrt{1-x} \pm i\sigma_Y\sqrt{x}$, as follows. Qubits q_1 and q_2 constitute the working substance, while qubits q_0 and q_3 are employed as ancillae to prepare the engine in the initial thermal state $\rho_1^0 \otimes \rho_2^0$, and emulate the actions of the hot and cold environments, respectively. This initial state is prepared by means of a rotation gate $R_x(\theta_i)$ in the ancillae and a CNOT gate between the ancillae and the qubits $i = A$ and B [q_1, q_2 in box 1, Fig. 1(b)]. The rotation angles are associated with the effective temperature of each qubit and with the correlation parameter α as follows:

$$\theta_A = \arccos\sqrt{p_-}, \quad \theta_B = \arccos\sqrt{p_+}, \tag{3}$$

$$p_\pm = \frac{1}{2}\left(p_A + p_B \pm \sqrt{(p_B - p_A)^2 + 4\alpha^2}\right), \tag{4}$$

$$\frac{\varepsilon_B}{\varepsilon_A} = \frac{\beta_A \ln(p_B \mathcal{Z}_B)}{\beta_B \ln(p_A \mathcal{Z}_A)}, \tag{5}$$

where $p_i = \exp(-\beta_i\varepsilon_i)/\mathcal{Z}_i$ and $\varepsilon_B/\varepsilon_A$ gives the qubits energy-gap ratio.

In the present implementation, the initial correlation in the working substance (q_1 and q_2) is achieved by a CNOT gate framing one controlled $U_-(x)$ gate, $x = x(\alpha) = (p_A - p_B)/(p_+ - p_-) + 1/2$, as shown in Fig. 1(b) (box 3) [66], and α should satisfy $\alpha \leqslant 1/(\mathcal{Z}_A\mathcal{Z}_B)$ to fulfill that the system's density operator is a positive semi-definite. We also produced the same reduced correlated state of the working substance in the ancillary qubits q_0 and q_3, through box 2 of Fig. 1(b), in order to have a copy of the initial correlated state at the circuit end, thus having an abridged measurement strategy. After boxes 2 and 3 [Fig. 1(b)], the working substance is in the state given by Eq. (1). Two distinct scenarios are identified: (i) $\alpha = 0$, the qubits are initially uncorrelated, and (ii) $\alpha \neq 0$, the bipartite state is initially correlated. The partial SWAP operation, stroke 2, can be effectively implemented through a quantum circuit composed by two CNOT gates framing one controlled-gate $U_{+}(\lambda)$ [Fig. 1(b), box 4]. For $\lambda = 1$, we have a full SWAP between the qubit states, while for $\lambda = 0$ there is no operation at all between such qubits. The partial SWAP takes place at a time τ, with $0 < \tau < \pi/(2J)$. We finally measure all qubits in their respective $(\sigma_Z^{(i)})$ energy basis.

III. QUANTUM-ENGINE NONEQUILIBRIUM-THERMODYNAMICS QUANTIFIERS

For the aforementioned cycle, we calculate the mean energies involved in the whole process: the average values for the work, $\langle W\rangle = \mathrm{Tr}[(\rho_{AB}^{f} - \rho_{AB}^{0})\mathcal{H}_{AB}]$ (that takes place in stroke 2) and the heat contributions from the hot ($\langle Q_A\rangle$) and cold ($\langle Q_B\rangle$) environments, $\langle Q_i\rangle = -\mathrm{Tr}[(\rho_i^{f} - \rho_i^{0})\mathcal{H}_i]$, where $\rho_{A(B)}^{f} = \mathrm{Tr}_{B(A)}(\rho_{AB}^{f}) = \mathrm{Tr}_{B(A)}(\mathcal{U}_\tau \rho_{AB}^{0} \mathcal{U}_\tau^{\dagger})$ is the final out-of-equilibrium reduced state for qubit A (B) after stroke 2. We obtain

$$\langle W\rangle = 2(\varepsilon_B - \varepsilon_A) f(\Delta\nu, \lambda, \alpha), \tag{6}$$

$$\langle Q_A\rangle = 2\varepsilon_A f(\Delta\nu, \lambda, \alpha), \tag{7}$$

$$\langle Q_B\rangle = -2\varepsilon_B f(\Delta\nu, \lambda, \alpha), \tag{8}$$

with $f(\Delta\nu, \lambda, \alpha) = \frac{\sinh(\Delta\nu)}{\mathcal{Z}_A\mathcal{Z}_B}\lambda + 2\alpha\sqrt{\lambda(1-\lambda)}$, where $\Delta\nu = (\varepsilon_B\beta_B - \varepsilon_A\beta_A)/2$. Since the total energy is conserved, Eq. (6) to (8) fulfill energy conservation, i.e., $\langle W\rangle = -(\langle Q_A\rangle + \langle Q_B\rangle)$. These results for the correlated case ($\alpha \neq 0$) are plotted in Fig. 2(b) and as the continuous curves in Fig. 2(d) (see also Fig. 3). For comparison, in Figs. 2(a) and 2(c), we plot the corresponding energies in the absence of initial correlations ($\alpha = 0$).

We characterized the performance of the quantum engine by varying the energy gap ratio $\varepsilon_B/\varepsilon_A$, setting $\beta_B = 2\beta_A$, and fixing the SWAP parameter to $\lambda = 0.6$ (other values are considered in Fig. 3). For the correlated initial state we considered α's maximum value, $\alpha_{\max} = 1/(\mathcal{Z}_A\mathcal{Z}_B)$.

In Figs. 2(a) and 2(b), we plot the parameters' diagram for temperature and energy gap ratios $\{\beta_B/\beta_A, \varepsilon_B/\varepsilon_A\}$ required for work extraction for both, initially uncorrelated, and correlated scenarios. The dashed curve in the diagram for the case without initial correlations, Fig. 2(a), separates the regions for which the system can work as a refrigerator (work injection) or as a heat engine (work extraction). In contrast, for initially correlated qubits [Fig. 2(b)], work injection gets suppressed in the whole gap ratio $\varepsilon_B/\varepsilon_A < 1$, for all $\beta_A < \beta_B$, and work extraction becomes much higher; the maximal extracted work can be seen, e.g., for $\beta_B \gtrsim 3\beta_A$ and $0.2 \lesssim \varepsilon_B/\varepsilon_A \lesssim 0.5$ [Fig. 2(b)].

In Figs. 2(c) and 2(d), we plot the mean energy (re-scaled) quantities, work ($\langle W\rangle$, black dots) and heat from the hot ($\langle Q_A\rangle$, red dots) and cold ($\langle Q_B\rangle$, blue dots) environments obtained from the experimental runs in the quantum processor. The error bars were estimated using the standard deviation of the measured data in the quantum processor. Three operational regimes [65] appear in the initially uncorrelated qubits scenario [Fig. 2(c)]: refrigerator ($0 < \varepsilon_B/\varepsilon_A < 1/2$), heat engine ($1/2 < \varepsilon_B/\varepsilon_A < 1$), and heat accelerator ($\varepsilon_B/\varepsilon_A > 1$). However, when the qubits are initially correlated, the partial SWAP engine only exhibits two operational modes: heat engine ($0 < \varepsilon_B/\varepsilon_A < 1$) and heat accelerator ($\varepsilon_B/\varepsilon_A > 1$) [Fig. 2(d)].

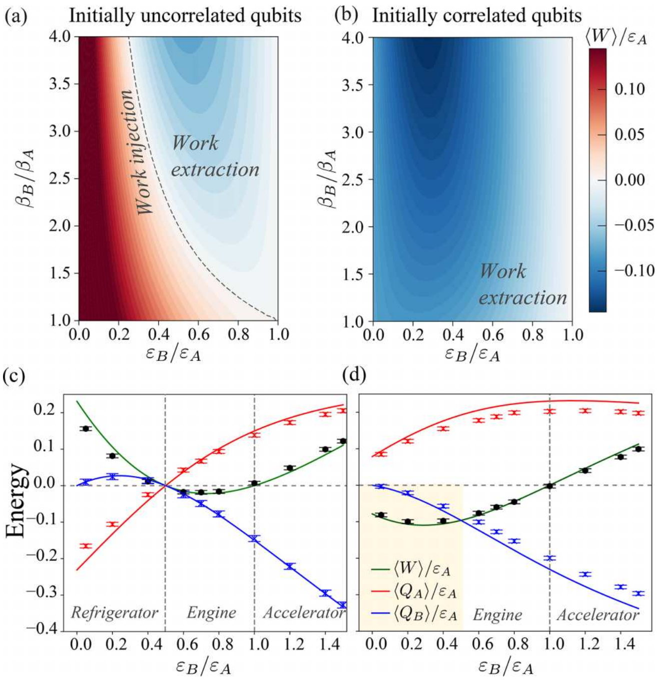

FIG. 2. Parameters phase diagram for engine operation mode: (a) initially uncorrelated qubits, work extraction is only allowed for parameter ratios $\{\beta_B/\beta_A, \varepsilon_B/\varepsilon_A\}$ above the dashed curve (blue region); and (b) initially correlated qubits, work extraction is allowed for all $0 \leqslant \varepsilon_B/\varepsilon_A < 1$, $\beta_A < \beta_B$. Experimental results for the rescaled average work ($\langle W\rangle/\varepsilon_A$), and heat from the hot ($\langle Q_A\rangle/\varepsilon_A$) and cold ($\langle Q_B\rangle/\varepsilon_A$) reservoirs for (c) initially uncorrelated qubits, and (d) initially correlated qubits; in all experimental runs in the quantum processor, we set $\beta_B = 2\beta_A$, $\lambda = 0.6$, and $\alpha_{\max} = 1/(\mathcal{Z}_A\mathcal{Z}_B)$. The error bars were estimated using the standard deviation of the measured data. The solid curves correspond to the theoretical prediction.

In the engine operation mode, quantum correlations boost the amount of work that can be extracted, making it at its maximum about an order of magnitude larger than the one obtained in the absence of initial qubit correlations. As already explained above, this result has also been verified for other λ values (see Fig. 3). In Figs. 2(c), 2(d), and 3, we find a very good agreement between the quantum-processor-implementation results and the corresponding theoretical prediction from Eqs. (6) to (8) (solid curves). Furthermore, quantum correlations enlarge the $\varepsilon_B/\varepsilon_A$ values' window where work extraction is possible.

In Fig. 3 the average work and heat from the hot and cold environments, for different λ values are plotted. As established above, Fig. 3(a) shows the three different modes of operation of the SWAP quantum engine that are available if we consider initially uncorrelated qubits ($\lambda = 0$). The engine mode occurs for $0.5 < \varepsilon_B/\varepsilon_A < 1$. Otherwise, for initially correlated qubits, the engine mode expands its range to $0.0 < \varepsilon_B/\varepsilon_A < 1$, as it is shown in Figs. 3(b)–3(d), $\lambda = 0.8$, 0.6, and 0.2, respectively. The lower the λ parameter the greater the amount of extracted work. In fact, executing a full SWAP ($\lambda = 1$) in the engine would erase the advantage due to its quantum correlations hence obtaining the same result as in the absence of initial correlations.

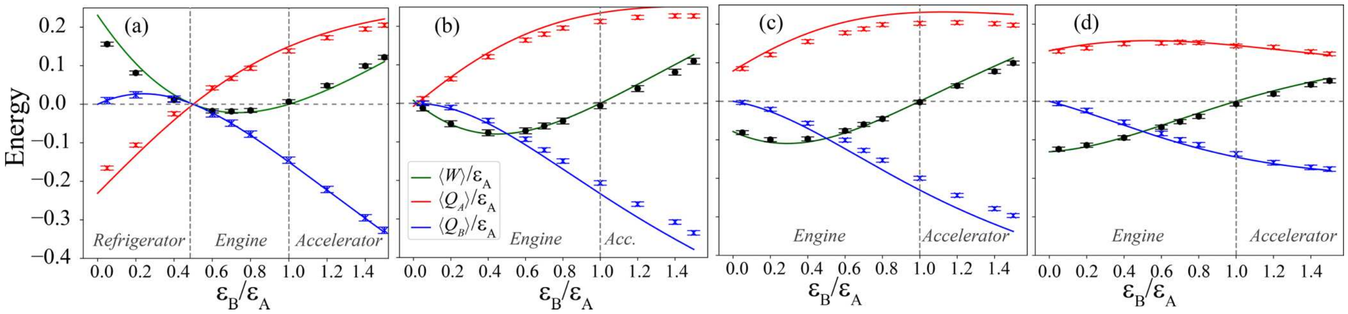

FIG. 3. Quantum-processor-implementation results for the average work, and heat from the hot ($\langle Q_A\rangle$) and cold ($\langle Q_B\rangle$) reservoirs for (a) initially uncorrelated qubits ($\lambda = 0$), and initially correlated qubits: (b) $\lambda = 0.8$, (c) 0.6, and (d) 0.2. In all runs in the quantum processor, $\beta_B = 2\beta_A$ and $\alpha_{\max} = 1/(\mathcal{Z}_A\mathcal{Z}_B)$. The error bars were estimated using the standard deviation of the measured data. The solid curves are obtained from our theoretical predictions from Eqs. (6) to (8) and numerical simulations.

From Eqs. (6) and (7), it is straightforward to obtain the SWAP engine efficiency,

$$\eta = -\frac{\langle W\rangle}{\langle Q_A\rangle} = 1 - \frac{\varepsilon_B}{\varepsilon_A}. \tag{9}$$

For qubit energies such that $\frac{\varepsilon_B}{\varepsilon_A} = \frac{\beta_A}{\beta_B}$, the quantum engine achieves the standard Carnot limit,

$$\eta_{\text{Carnot}} \equiv 1 - \frac{\beta_A}{\beta_B}. \tag{10}$$

IV. QUANTUM HEAT ENGINE EXPERIMENTAL SETUP

Here we give further details about the quantum processor implementation of a quantum heat engine and corresponding data analysis. For the implementation and characterization of the quantum heat engine, we ran several experiments on the five-qubit *ibmq_manila* quantum processor [63]. Below we experimentally demonstrate the performance enhancement of a correlated SWAP heat engine and confirm our theoretical predictions.

For each run in the quantum processor, we implemented the quantum circuit depicted in Fig. 1(b) and collected the qubits statistics over a sample of size 20 000. We performed the experiment for different values of the partial SWAP parameter λ. Additionally, for each λ, we ran ten experiments with the aforementioned sample size in order to see the fluctuations of the experimental setup. From these, we estimated the error propagation, using the standard deviation. Each circuit run is determined by the correlation (α) and thermalization (λ) parameters.

In Fig. 4, we outline the transpiled circuit that has been implemented following the topology and optimization of *ibmq_manila*. This corresponds to the engine thermodynamic cycle portrayed in the circuit of Fig. 1(b). The correlated SWAP engine implementation parameters (see Table I) have energy-gap ratio $\varepsilon_B/\varepsilon_A$, and angles θ_A and θ_B, with $p_\pm$ and p_i as given in Eqs. (3) to (5). Here,

$$\phi_A = \arcsin\sqrt{x(\alpha)}, \tag{11}$$

$$\phi_B = \phi_A - \arcsin\sqrt{\lambda}, \tag{12}$$

$$x(\alpha) = (p_A - p_B)/(p_+ - p_-) + 1/2, \tag{13}$$

where $x(\alpha)$ and λ give the correlation and partial swap parameters, respectively. In Table I, we display the experimental angles used in all the runs in the quantum processor here reported.

In the transpiled circuit (Fig. 4), three basic gates are used; R_z rotations, $\sqrt{X}$ and CNOT, in order to parallel implement the original quantum circuit of Fig. 1(b). We resort to the gating and decoherence times for *ibmq_manila* [63] as figures of merit to check that the coherence properties required in the implementation of the quantum thermodynamic cycle are guaranteed. Clearly, relaxation (T_1) and decoherence (T_2) times are about three orders of magnitude longer than the qubits' gating times. These times are reported in Table II.

The last column gives the execution times of the "*i_j*" two-qubit gates according to the *ibmq_manila* topology ($i, j = 0, 1, \ldots, 4$). By assuming that each gate takes its longest possible execution time (∼500 ns), we can overestimate

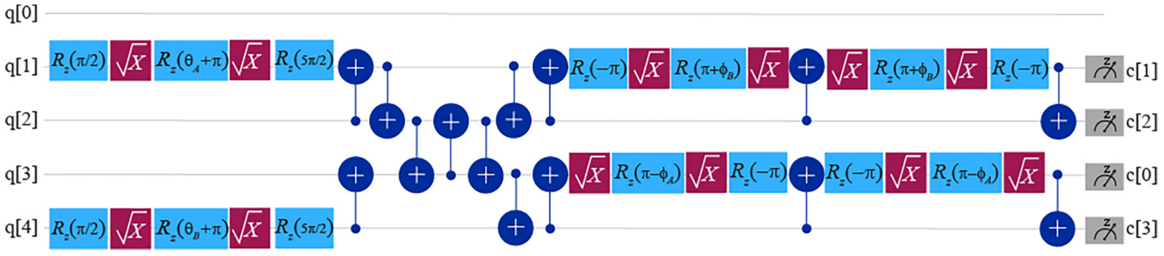

FIG. 4. Schematic representation of the transpiled circuit implemented by three basis gates: R_z rotations, $\sqrt{X}$, and CNOT. The circuit depth or layers of quantum gates are executed in parallel according to *ibmq_manila* topology to achieve the computation indicated in the original circuit of Fig. 1(b). The $q[i]$ input labeling indicates the physical qubits used by the five-qubit processor and the circuit output $c[i]$ represents the classical data where the measurement result is recorded.

TABLE I. Parameters used in the transpiled circuit displayed in Fig. 4 for the engine implementation in a quantum processor.

Engine implementation experimental parameters						
				$\lambda = 0.2$	$\lambda = 0.6$	$\lambda = 0.8$
$\varepsilon_B/\varepsilon_A$	θ_A(rad)	θ_B(rad)	ϕ_A(rad)	ϕ_B(rad)	ϕ_B(rad)	ϕ_B(rad)
0.05	2.41	1.34	2.57	0.10	−0.32	−0.54
0.20	2.47	1.45	2.50	0.17	−0.25	−0.47
0.40	2.55	1.56	2.41	0.27	−0.15	−0.37
0.60	2.64	1.69	2.31	0.37	−0.05	−0.27
0.70	2.67	1.74	2.26	0.42	−0.001	−0.22
0.80	2.71	1.79	2.21	0.467	0.05	−0.17
1.00	2.78	1.86	2.12	0.56	0.14	−0.08
1.20	2.84	1.92	2.03	0.65	0.22	0.002
1.40	2.89	1.96	1.96	0.72	0.30	0.08
1.50	2.91	1.97	1.92	0.75	0.33	0.11

the runtime of the full circuit to approximately 11 μs, which is shorter than the shortest T_2 time reported in Table II.

In Fig. 5, we plot the average work and efficiency for (a) and (c) initially uncorrelated qubits, (b) and (d) initially correlated qubits. The blue dots give the results of 10 experiments for each energy gap ratio value shown in the figure. Each dot is obtained by running the circuit Fig. 4 with 20 000 shots, using the parameters given in Table I. Figures 5(a) and 5(b) demonstrate that the extractable work (negative work) under initially correlated qubits is larger (about an order of magnitude larger at its maximum) than the one obtained in the absence of initial qubit correlations. In Figs. 5(c) and 5(d), we show the efficiency obtained for the experimental implementation of the thermal machine. This is in agreement with the criterion given below [see Eqs. (16) and (17)]: efficiency for uncorrelated initial qubits remain below the standard Carnot limit, while initially correlated qubits may allow for a boost in efficiency, with values well above the Carnot limit.

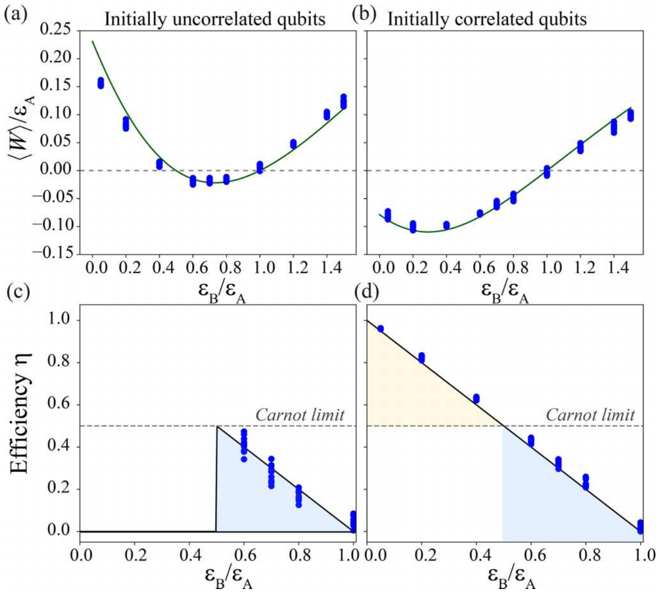

FIG. 5. Quantum-processor-implementation results for the average work and efficiency, considering (a) and (c) initially uncorrelated qubits; (b) and (d) initially correlated qubits. The blue dots indicate the realization of 10 different experiments for each $\varepsilon_B/\varepsilon_A$ value, and each one performed with 20 000 shots. The full lines in (c) and (d) correspond to the theoretical prediction. In all the figures, $\lambda = 0.6$, $\beta_B = 2\beta_A$, and $\alpha_{\max} = 1/(\mathcal{Z}_A\mathcal{Z}_B)$.

TABLE II. Calibration data for the qubits involved in the generation of the heat engine at the five-qubit *ibmq_manila* quantum processor (Fig. 4).

ibmq_manila calibration data			
Qubit	T_1 (μs)	T_2 (μs)	Gate time (ns)
q_0	177.13	78.73	0_1: 277.33
q_1	186.02	75.55	1_2: 469.33 1_0: 312.89
q_2	136.19	22.30	2_3: 355.56 2_1: 504.88
q_3	184.82	46.64	3_4: 334.22 3_2: 391.11
q_4	122.91	43.53	4_3: 298.67

V. BOOSTING QUANTUM ENGINE EFFICIENCY BY QUANTUM CORRELATIONS

The mutual information $I(A:B) = S_A + S_B - S_{AB}$ gives a measure of the total correlations between systems A and B, where $S_i = -\mathrm{Tr}_i(\rho_i \ln \rho_i)$ is the von Neumann entropy of state ρ_i. We next derive an analytical expression for the SWAP engine efficiency. Such efficiency involves an information-to-energy trade-off relation written in terms of the single-cycle variation of the mutual information between qubits A and B, $\Delta I(A:B) = \Delta S_A + \Delta S_B$ (where $\Delta S_i = S(\rho_i^f) - S(\rho_i^0)$) and of the entropy production cycle, $\Sigma_{\mathrm{eng}} = D[\rho_A^f||\rho_A^0] + D[\rho_B^f||\rho_B^0]$. Here, $D[\rho||\sigma] = \mathrm{Tr}[\rho(\ln\rho - \ln\sigma)]$ is the Kullback-Leibler divergence [1]. For the cycle, we arrive at the following generalized efficiency (see Appendix B):

$$\eta = \eta_{\mathrm{Carnot}} - \frac{\Sigma_{\mathrm{eng}} + \Delta I(A:B)}{\beta_B\langle Q_A\rangle}. \tag{14}$$

Equation (14) can be applied to all cycles based on bipartite working substance (of any dimension) when work and heat exchanges are performed in different strokes. Let us now introduce an efficiency booster quantifier $\mathcal{B}_{\mathcal{E}}$,

$$\mathcal{B}_{\mathcal{E}} \equiv \frac{\Sigma_{\mathrm{eng}} + \Delta I}{\beta_B\langle Q_A\rangle}, \tag{15}$$

which tracks the direct competition between entropy production and correlations consumption.

A. Engine efficiency criterion

Equation (14) implies that there may exist efficiencies above Carnot, $\eta > \eta_{\mathrm{Carnot}}$, depending on the sign of ΔI, with

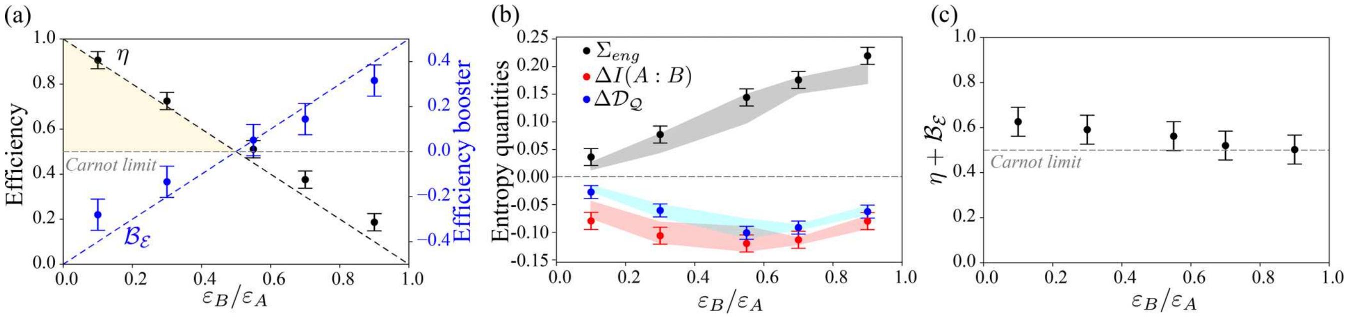

FIG. 6. Experimental results for the correlated SWAP quantum heat engine implementation; figures of merit: (a) efficiency and booster, (b) entropy production, variation of mutual information and of quantum discord, and (c) test of the generalized second-law limit for efficiency, which must satisfy $\eta + \mathcal{B}_\mathcal{E} = \eta_{\text{Carnot}} = 1/2$. The black and blue dashed lines in (a) correspond to the theoretical expectation for the correlated SWAP engine efficiency and efficiency booster, respectively. The shaded areas in (b) denote the theoretical results but calculated with the actual initial experimental states (instead of the ideal ones) of the various experimental runs. In all experiments, we set $\beta_B = 2\beta_A$, $\lambda = 0.6$, and $\alpha_{\max} = 1/(\mathcal{Z}_A\mathcal{Z}_B)$. The error bars were estimated using the standard deviation of the measured data.

the following engine efficiency criterion arising

$$\mathcal{B}_\mathcal{E} < 0, \quad \eta > \eta_{\text{Carnot}}, \tag{16}$$

$$\mathcal{B}_\mathcal{E} \geqslant 0, \quad \eta \leqslant \eta_{\text{Carnot}}. \tag{17}$$

Equation (14) can be seen as a quantum generalization of the second law efficiency and expression (16) is the condition for performance over the classical limit to occur, and indeed it is satisfied in Fig. 6(a). This result arises since the variation of mutual information ΔI is always negative, and there is a trade-off with the always positive entropy production Σ_{eng} [see Fig. 6(b)]. The variation of $\Delta I = \Delta\mathcal{D}_\mathcal{Q} + \Delta\mathcal{C}$, where $\mathcal{D}_\mathcal{Q}$ quantifies purely quantum correlations (here given by the quantum discord [67]), and $\mathcal{C}$ represents classical correlations, demonstrates that there is a consumption of quantum correlations during the thermodynamic cycle. For $\varepsilon_B/\varepsilon_A < 1/2$, this makes $\Sigma_{\text{eng}} < |\Delta I(A:B)|$ and hence $\mathcal{B}_\mathcal{E} < 0$, which in turn implies $\eta > \eta_{\text{Carnot}}$ in Eq. (14).

For the calculation of the quantum correlations we have used the geometrical quantum discord $\mathcal{D}_\mathcal{Q}$ for a two-qubit X state [69,70], which can be written in terms of the elements of the density matrix as

$$\mathcal{D}_\mathcal{Q} = [k_1 - 2k_2 + 4z^2 - \max(k_1 - 2k_2, 2z^2)], \tag{18}$$

where $k_1 = a^2 + b^2 + c^2 + d^2$ and $k_2 = ac + bd$.

The emergence of condition (16) depends on a proper choice of initially correlated states and of the driving Hamiltonian in the stroke 2. It only arises if $\mathcal{B}_\mathcal{E} < 0$. Otherwise, $\eta \leqslant \eta_{\text{Carnot}}$ [Eq. (17)]; $\mathcal{B}_\mathcal{E} \geqslant 0$ also describes engine operation for initially uncorrelated qubits [Fig. 2(a)]: entropy production is always greater or equal than variation of mutual information. An experimental verification of the engine efficiency criterion Eqs. (16) and (17) (see Figs. 5–7) is provided below.

B. Experimental demonstration of performance boosting in the correlated SWAP heat engine

In Fig. 6, we plot the quantum-processor-implementation results for the efficiency, the entropy and the generalized second law related quantities as a function of the energy gap ratio. These quantifiers have been obtained by using quantum state tomography (QST), as detailed below. The efficiency η (black dots) and the efficiency booster $\mathcal{B}_\mathcal{E}$ (blue dots) are displayed in Fig. 6(a). The plotted error bars were estimated

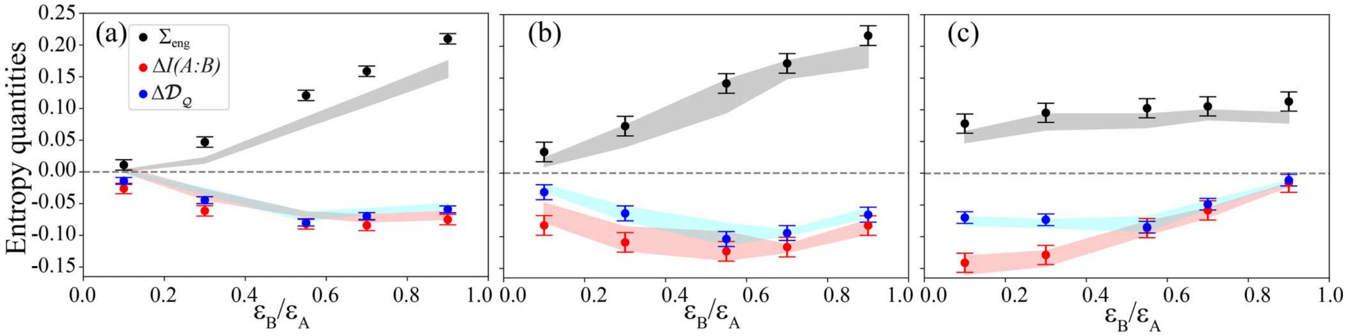

FIG. 7. Entropy and correlation quantities during the thermodynamic cycle: (a) $\lambda = 0.8$, (b) $\lambda = 0.6$, and (c) $\lambda = 0.2$. Experimental data in black, blue, and red correspond to the entropy production, variation of quantum discord and variation of mutual information, respectively. In all runs in the quantum processor, the temperature relation $\beta_B = 2\beta_A$ and the correlation factor $\alpha_{\max} = 1/(\mathcal{Z}_A\mathcal{Z}_B)$. The shaded areas denote the theoretical results calculated with the actual initial experimental states (instead of the ideal one), see, e.g., Fig. 8. The error bars were estimated using the standard deviation of the measured data.

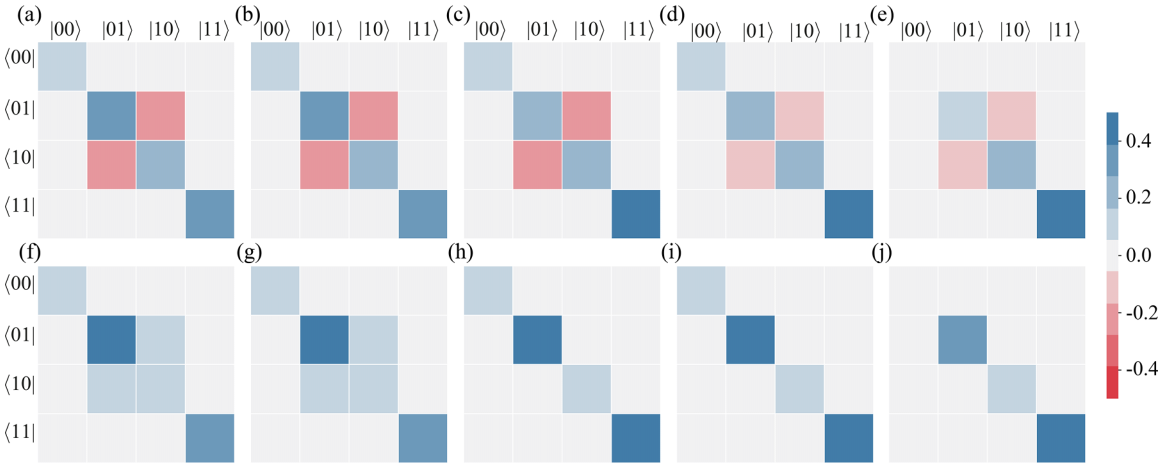

FIG. 8. Quantum state tomography of the two-bit working substance for the initially correlated state (upper row) and corresponding final state (lower row) for $\lambda = 0.6$ and for the following qubits energy gap ratios $\varepsilon_B/\varepsilon_A$: (a) and (f) 0.10; (b) and (g) 0.30; (c) and (h) 0.55; (d) and (i) 0.70; (e) and (j) 0.90. Data shown represent the result over 20 000 shots for each circuit used in one of the QST implementations. Re(ρ) denotes the real values of the density matrix (the corresponding imaginary part entries are of the order of 10^{-3}, not shown).

as in Fig. 2. The booster $\mathcal{B}_\mathcal{E}$ reaches negative values hence the efficiencies go above the Carnot limit, $\eta_{\text{Carnot}} = 0.5$, in agreement with our theoretical findings (solid lines). In Fig. 6(b), we plot the entropy production (black dots), the variation of mutual information (red dots), and of quantum discord (blue dots) obtained in the quantum processor implementation. For $\varepsilon_B/\varepsilon_A < 0.5$, we obtain $|\Delta I(A:B)| > \Sigma_{\text{eng}}$ and since ΔI is always negative, $\mathcal{B}_\mathcal{E} < 0$ and the SWAP engine efficiency surpasses the standard Carnot limit $\eta > \eta_{\text{Carnot}}$, which is in perfect agreement with Fig. 6(a) and with the criterion Eq. (16).

We make explicit the role of the measured correlations (both quantum and classical), by plotting $\Delta I = \Delta\mathcal{D}_Q + \Delta\mathcal{C}$ and $\Delta\mathcal{D}_Q$, during the thermodynamic cycle [see the two lower curves of Fig. 6(b)]. Here, the variation of quantum discord closely follows that of mutual information and both are always negative. This means that while entropy production increases, both variations in classical and quantum correlations are consumed during the cycle. The larger correlations consumption is of purely quantum origin, and come from the discord. These results have been further verified and plotted for Σ_{eng}, ΔI and $\Delta\mathcal{D}_Q$ in Fig. 7, for other values of λ. The shaded areas in Fig. 6(b) represent the theoretical results calculated with the actual initial states in the quantum processor (instead of the ideal one) of the various runs. The theoretical predictions are in very good agreement with the implementation results.

Figure 6(c) shows the quantum-processor-implementation results for a verification of the generalized efficiency formula as a function of the qubits' energy-gap ratio. The black dots give the results for the sum of the engine efficiency and the booster $\eta + \mathcal{B}_\mathcal{E}$, as averaged measurements following the qubits statistics from collected data from 20 000 runs. We find that the generalized second law limit measured with the *ibmq_manila* quantum processor is at most within two standard deviations from the analytical result Eq. (14), thus verifying, with Fig. 6(b), the quantum origin of the working thermodynamical principle for enhancing the efficiency of the correlated SWAP quantum heat engine.

C. Entropy related quantities and quantum state tomography

In Fig. 7, we plot the variation of entropic and correlation quantities as a function of $\varepsilon_B/\varepsilon_A$, namely the variation of the engine entropy production Σ_{eng}, of the mutual information ΔI and of the quantum discord $\mathcal{D}_Q$, for (a) $\lambda = 0.8$, (b) 0.6, and (c) 0.2. Figure 7 further demonstrates that the variation of mutual information is mostly due to the consumption of quantum correlations between the qubits. It also confirms that for initially correlated systems $|\Delta I|$ may be greater than Σ_{eng}, leading to a correlation boosting of the engine efficiency.

For the quantum state tomography (QST) implementation required in this analysis, we have used a module in the QISKIT-IGNIS library [68]. For a complete QST of a two-qubits state, nine circuits are needed. The result for each circuit is averaged over 20 000 shots and, additionally, in order to average over the system fluctuations, we repeat the process five times for the initial state and five times for the final one. In Figs. 8(a)–8(e), we show the QST result for the initially correlated state ρ^0_{AB}, considering $\varepsilon_B/\varepsilon_A = 0.10,\ 0.30,\ 0.55,\ 0.70,$ and 0.90, respectively. In the same way, in Figs. 8(f)–8(j), we give the QST result for the final state, with $\lambda = 0.6$ and $\varepsilon_B/\varepsilon_A = 0.10,\ 0.30,\ 0.55,\ 0.70,$ and 0.90, respectively. Similar results were obtained for $\lambda = 0.2, 0.8$ (not shown). In the computational basis, the qubits density matrix can then be approximated as

$$\rho = \begin{pmatrix} a & 0 & 0 & 0 \\ 0 & b & z & 0 \\ 0 & z & c & 0 \\ 0 & 0 & 0 & d \end{pmatrix}. \tag{19}$$

VI. SUMMARY

In summary, the limits posed by the second law of thermodynamics may be affected by the presence of initial quantum correlations in the working fluid of a thermal machine, leading to efficiency higher than the Carnot standard limit and to a boost in the extractable work in each cycle. A criterion for the construction of such enhanced thermodynamic feature is given in terms of a trade-off between entropy production and quantum correlations consumption during the implemented thermal machine's cycle. The design of thermal machines that use extra resources based on quantum correlations highlight the need for a revision of the standard thermodynamics limits. In this framework, the energetic cost of building initial correlations should not be included in the efficiency definition. This is in line with the practice of not including costs related to the production of (hot) heat sources in classical internal-combustion engines (e.g., fuel production/refining, etc.). Our results with an IBM quantum processor clearly demonstrate that the effect we propose allows to obtain advantages in thermal tasks using available quantum technology.

ACKNOWLEDGMENTS

M.H. and J.H.R. acknowledge the financial support from MinCiencias (Colombia) through a Postdoctoral Fellowship Award (Grant No. 270-2021/CI 71295) and the Norwegian Ministry of Education and Research, through the QTEC-NOS consortium (NORPART 2021-10436/CI 71331). M.H. thanks Universidad Autónoma de Occidente (Colombia) for partial financial support. R.M.S. also acknowledges CNPq, FAPESP (Brazil), and Ministry of Science and Technology (China), through the High-End Foreign Expert Program (Grant No. G2021016021L). I.D. acknowledges the kind hospitality of the Instituto de Física de São Carlos, University of São Paulo, São Carlos (Brazil). We also acknowledge the use of *ibmq_manila* quantum processor of IBM Quantum services [63].

APPENDIX A: ABOUT ENERGY EXCHANGE, CORRELATIONS PRODUCTION AND EFFICIENCY

Here we show the effect of taking into account the initial-state correlation production in the thermodynamic cycle. To do so, we start from the state in stroke 1.1 [Fig. 1(a)]. Such a state, $\tilde{\rho}_A^0 \otimes \tilde{\rho}_B^0$, explicitly reads

$$\begin{pmatrix} p_+p_- & 0 & 0 & 0 \\ 0 & p_+(1-p_-) & 0 & 0 \\ 0 & 0 & p_-(1-p_+) & 0 \\ 0 & 0 & 0 & (1-p_+)(1-p_-) \end{pmatrix}. \tag{A1}$$

The populations of states $\tilde{\rho}_A^0$ and $\tilde{\rho}_B^0$ are chosen as $p_\pm = (p_A + p_B \pm \sqrt{(p_B - p_A)^2 + 4\alpha^2})/2$ to obtain the desired correlated state $\rho_{AB}^0 = \rho_A^0 \otimes \rho_B^0 + \chi_{AB}$, where p_- (p_+) denotes the ground state population of $\tilde{\rho}_A^0$ ($\tilde{\rho}_B^0$). Hence, ρ_{AB}^0 becomes

$$\begin{pmatrix} p_Ap_B - \alpha^2 & 0 & 0 & 0 \\ 0 & p_A(1-p_B) + \alpha^2 & \alpha & 0 \\ 0 & \alpha & p_B(1-p_A) + \alpha^2 & 0 \\ 0 & 0 & 0 & (1-p_A)(1-p_B) - \alpha^2 \end{pmatrix}, \tag{A2}$$

and the von Neumann entropy of $\rho_A^0 \otimes \rho_B^0 + \chi_{AB}$ is the same than that of $\tilde{\rho}_A^0 \otimes \tilde{\rho}_B^0$. In fact, using the expressions for $p_\pm$ and p_i, we obtain the same eigenvalues for both density operators, ρ_{AB}^0 and $\tilde{\rho}_A^0 \otimes \tilde{\rho}_B^0$:

$$\begin{aligned} \nu_1 &= \frac{1}{2}[p_A + p_B - 2p_Ap_B + 2\alpha^2 - \sqrt{(p_B - p_A)^2 + 4\alpha^2}], \\ \nu_2 &= (1 - p_A)(1 - p_B) - \alpha^2, \\ \nu_3 &= p_Ap_B - \alpha^2, \\ \nu_4 &= \frac{1}{2}[p_A + p_B - 2p_Ap_B + 2\alpha^2 + \sqrt{(p_B - p_A)^2 + 4\alpha^2}]. \end{aligned} \tag{A3}$$

From the initial state $\tilde{\rho}_A^0 \otimes \tilde{\rho}_B^0$, we calculate the heat and work as $\langle \tilde{Q}_i \rangle = -\text{Tr}[(\rho_i^f - \tilde{\rho}_i^0)\mathcal{H}_i]$ and $\langle \tilde{W} \rangle = \text{Tr}[(\rho_{AB}^f - \tilde{\rho}_A^0 \otimes \tilde{\rho}_B^0)\mathcal{H}_{AB}]$, respectively. In Fig. 9(a), the dashed lines correspond to the heat generation ($\langle \tilde{Q}_A \rangle/\epsilon_A$, pink area) and work production ($\langle \tilde{W}_A \rangle/\epsilon_A$, yellow area) when considering $\tilde{\rho}_A^0 \otimes \tilde{\rho}_B^0$ as the initial state. We see that $\langle \tilde{Q}_A \rangle$ and $\langle \tilde{W} \rangle$ are greater than $\langle Q_A \rangle$ and $\langle W \rangle$ (in absolute value), but the cycle efficiency when considering the correlation production $\tilde{\eta} = \langle \tilde{W} \rangle / \langle \tilde{Q}_A \rangle$ corresponds to the same one computed from the correlated state $\eta = \langle W \rangle / \langle Q_A \rangle$, as it is shown in Fig. 9(b). This is so because there is a compensation in the extra amounts obtained for the corresponding heat and work, as illustrated in the shaded areas of Fig. 9(a). These show the extra heat generation (pink area) and the correlation production cost (yellow area) due to the generation of correlations in the initial state.

APPENDIX B: DEMONSTRATION OF THE GENERALIZED SECOND-LAW LIMIT

Here we give a demonstration for the efficiency result Eq. (14). The entropy production of the correlated SWAP quantum engine can be expressed as the sum of two relative entropies that reads

$$\begin{aligned} D\big[\rho_A^f \| \rho_A^0\big] + D\big[\rho_B^f \| \rho_B^0\big] &= -\Delta S_A - \Delta S_B + \beta_A \text{Tr}\big[\big(\rho_A^f - \rho_A^0\big)\mathcal{H}_A\big] \\ &\quad + \beta_B \text{Tr}\big[\big(\rho_B^f - \rho_B^0\big)\mathcal{H}_B\big], \end{aligned} \tag{B1}$$

where ρ_i^f is the final out-of-equilibrium state for the qubit $i = A, B$. We simplify this equation by introducing

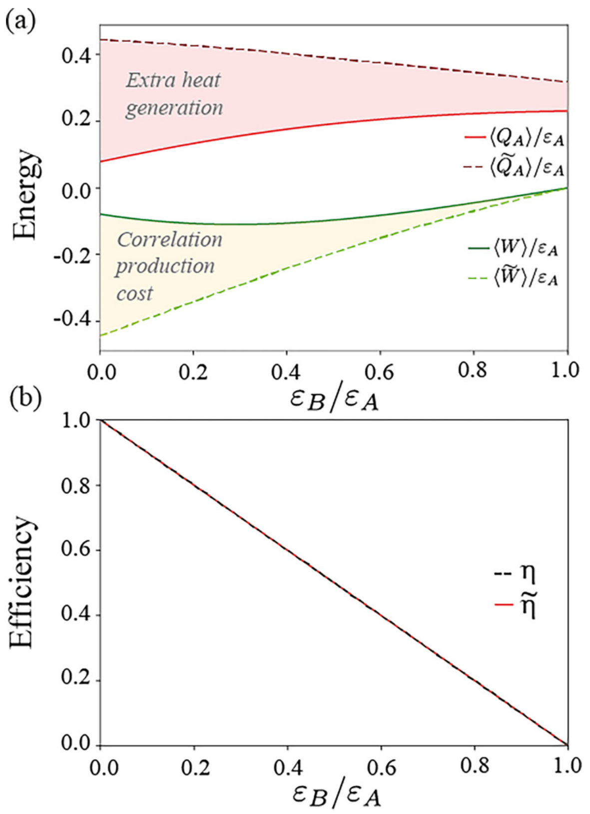

FIG. 9. (a) Average work $\langle \widetilde{W}\rangle/\varepsilon_A$, heat from the hot reservoir $\langle \widetilde{Q}_A\rangle/\varepsilon_A$, and (b) efficiency $\tilde{\eta}$, including in the cycle the initial-state correlation production. In the same graphs, we plot the corresponding quantities but now without including the initial-state correlation production step: $\langle W\rangle/\varepsilon_A$, $\langle Q_A\rangle/\varepsilon_A$, and η. We set $\beta_B = 2\beta_A$, $\lambda = 0.6$, and $\alpha_{\max} = 1/(\mathcal{Z}_A\mathcal{Z}_B)$.

$\langle Q_i\rangle = -\mathrm{Tr}[(\rho_i^f - \rho_i^0)\mathcal{H}_i]$, hence

$$\begin{aligned} D\big[\rho_A^f\|\rho_A^0\big] + D\big[\rho_B^f\|\rho_B^0\big] \\ = -\Delta S_A - \Delta S_B - \beta_A\langle Q_A\rangle - \beta_B\langle Q_B\rangle. \end{aligned} \tag{B2}$$

We use the fact that $\Delta I(A:B) = \Delta S_A + \Delta S_B$ to rewrite Eq. (S4) as $D[\rho_A^f\|\rho_A^0] + D[\rho_B^f\|\rho_B^0] = -\Delta I(A:B) - \beta_A\langle Q_A\rangle - \beta_B\langle Q_B\rangle$. This is equivalent to

$$\frac{D\big[\rho_A^f\|\rho_A^0\big] + D\big[\rho_B^f\|\rho_B^0\big] + \Delta I(A:B)}{\beta_B\langle Q_A\rangle} = -\frac{\beta_A}{\beta_B} - \frac{\langle Q_B\rangle}{\langle Q_A\rangle}. \tag{B3}$$

Energy conservation implies that the average values for the heat and work, $\langle Q_A\rangle + \langle Q_B\rangle + \langle W\rangle = 0$. The extracted work $\langle W_{\text{ext}}\rangle = -\langle W\rangle = \langle Q_A\rangle + \langle Q_B\rangle$ and the quantum heat engine efficiency $\eta = \langle W_{\text{ext}}\rangle/\langle Q_A\rangle$ reads

$$\eta = 1 - \frac{\beta_A}{\beta_B} - \frac{D\big[\rho_A^f\|\rho_A^0\big] + D\big[\rho_B^f\|\rho_B^0\big] + \Delta I(A:B)}{\beta_B\langle Q_A\rangle}, \tag{B4}$$

where $1 - \beta_A/\beta_B$ is the standard Carnot limit. Equation (B4) defines a generalized second law limit for bipartite quantum engine in the presence of initial correlations. As discussed in the main text, the efficiency booster $\mathcal{B}_{\mathcal{E}} \equiv (\Sigma_{\text{eng}} + \Delta I)/\beta_B\langle Q_A\rangle$ sets a criterion [Eq. (16)] for the enhancement of the engine's efficiency and extractable work (see Figs. 3, 5, and 7).

[1] *Thermodynamics in the Quantum Regime: Fundamental Aspects and New Directions*, edited by F. Binder, L. A. Correa, C. Gogolin, J. Anders, and G. Adesso (Springer International, Cham, Swtizerland, 2018).

[2] S. Deffner and S. Campbell, *Quantum Thermodynamics - An Introduction to the Thermodynamics of Quantum Information* (Morgan & Claypool, San Rafael, CA, 2019).

[3] R. Kosloff, Quantum thermodynamics: A dynamical viewpoint, Entropy **15**, 2100 (2013).

[4] J. Goold, M. Huber, A. Riera, L. del Rio, and P. Skrzypczyk, The role of quantum information in thermodynamics - a topical review, J. Phys. A: Math. Theor. **49**, 143001 (2016).

[5] S. Vinjanampathy and J. Anders, Quantum thermodynamics, Contemp. Phys. **57**, 545 (2016).

[6] F. Brandão, M. Horodecki, N. Ng, J. Oppenheim, and S. Wehner, The second laws of quantum thermodynamics, Proc. Natl. Acad. Sci. USA **112**, 3275 (2015).

[7] G. E. Crooks, Entropy production fluctuation theorem and the nonequilibrium work relation for free energy differences, Phys. Rev. E **60**, 2721 (1999).

[8] C. Jarzynski, Nonequilibrium equality for free energy differences, Phys. Rev. Lett. **78**, 2690 (1997).

[9] M. Esposito, U. Harbola and S. Mukamel, Nonequilibrium fluctuations, fluctuation theorems, and counting statistics in quantum systems, Rev. Mod. Phys. **81**, 1665 (2009).

[10] M. Campisi, P. Hänggi, and P. Talkner, Quantum fluctuation relations: Foundations and applications, Rev. Mod. Phys. **83**, 771 (2011).

[11] M. Herrera, J. P. S. Peterson, R. M. Serra, and I. D'Amico, Easy access to energy fluctuations in nonequilibrium quantum many-body systems, Phys. Rev. Lett. **127**, 030602 (2021).

[12] A. Auffèves, Quantum technologies need a quantum energy initiative, Phys. Rev. X Quantum **3**, 020101 (2022).

[13] T. Hugel, N. B. Holland, A. Cattani, L. Moroder, M. Seitz, and H. E. Gaub, Single-molecule optomechanical cycle, Science **296**, 1103 (2002).

[14] P. G. Steeneken, K. Le Phan, M. J. Goossens, G. E. J. Koops, G. J. A. M. Brom, C. van der Avoort, and J. T. M. van Beek, Piezoresistive heat engine and refrigerator, Nat. Phys. **7**, 354 (2011).

[15] V. Blickle and C. Bechinger, Realization of a micrometresized stochastic heat engine, Nat. Phys. **8**, 143 (2012).

[16] J.-P. Brantut, C. Grenier, J. Meineke, D. Stadler, S. Krinner, C. Kollath, T. Esslinger, and A. Georges, A thermoelectric heat engine with ultracold atoms, Science **342**, 713 (2013).

[17] J. Roßnagel, O. Abah, F. Schmidt-Kaler, K. Singer, and E. Lutz, Nanoscale heat engine beyond the carnot limit, Phys. Rev. Lett. **112**, 030602 (2014).

[18] H. Thierschmann, R. Sánchez, B. Sothmann, F. Arnold, C. Heyn, W. Hansen, H. Buhmann, and L. W. Molenkamp, Three-terminal energy harvester with coupled quantum dots, Nat. Nanotechnol. **10**, 854 (2015).

[19] J. Roßsnagel, S. T. Dawkins, K. N. Tolazzi, O. Abah, E. Lutz, F. Schmidt-Kaler, and K. Singer, A single-atom heat engine, Science **352**, 325 (2016).

[20] F. Schmidt, A. Magazzú, A. Callegari, L. Biancofiore, F. Cichos, and G. Volpe, Microscopic engine powered by critical demixing, Phys. Rev. Lett. **120**, 068004 (2018).

[21] Y. Zou, Y. Jiang, Y. Mei, X. Guo, and S. Du, Quantum heat engine using electromagnetically induced transparency, Phys. Rev. Lett. **119**, 050602 (2017).

[22] R. J. de Assis, T. M. de Mendonça, C. J. Villas-Boas, A. M. de Souza, R. S. Sarthour, I. S. Oliveira and N. G. de Almeida, Efficiency of a quantum otto heat engine operating under a reservoir at effective negative temperatures, Phys. Rev. Lett. **122**, 240602 (2019).

[23] J. Klatzow, J. Becker, P. Ledingham, C. Weinzetl, K. Kaczmarek, D. Saunders, J. Nunn, I. Walmsley, R. Uzdin, E. Poem, Experimental demonstration of quantum effects in the operation of microscopic heat engines, Phys. Rev. Lett. **122**, 110601 (2019).

[24] J. P. S. Peterson, T. B. Batalhão, M. Herrera, A. M. Souza, R. S. Sarthour, I. S. Oliveira, and R. M. Serra, Experimental characterization of a spin quantum heat engine, Phys. Rev. Lett. **123**, 240601 (2019).

[25] T. Denzler, J. F. G. Santos, E. Lutz, and R. M. Serra, Nonequilibrium fluctuations of a quantum heat engine, arXiv:2104.13427 v1.

[26] A. Solfanelli, A. Santini, and M. Campisi, Experimental verification of fluctuation relations with a quantum computer, PRX Quantum **2**, 030353 (2021).

[27] N. M. Myers, O. Abah, and S. Deffner, Quantum thermodynamic devices: From theoretical proposals to experimental reality, AVS Quantum Sci. **4**, 027101 (2022).

[28] G. Lebon, D. Jou, and J. Casas-Vázques, *Understanding Non-Equilibrium Thermodynamics: Foundations, Applications, Frontiers* (Springer-Verlag, Berlin, 2008).

[29] T. B. Batalhão, A. M. Souza, L. Mazzola, R. Auccaise, R. S. Sarthour, I. S. Oliveira, J. Goold, G. De Chiara, M. Paternostro, and R. M. Serra, Experimental reconstruction of work distribution and study of fluctuation relations in a closed quantum system, Phys. Rev. Lett. **113**, 140601 (2014).

[30] T. B. Batalhão, A. M. Souza, R. S. Sarthour, I. S. Oliveira, M. Paternostro, E. Lutz, and R. M. Serra, Irreversibility and the arrow of time in a quenched quantum system, Phys. Rev. Lett. **115**, 190601 (2015).

[31] P. A. Camati, J. P. S. Peterson, T. B. Batalhão, K. Micadei, A. M. Souza, R. S. Sarthour, I. S. Oliveira, and R. M. Serra, Experimental rectification of entropy production by Maxwell's demon in a quantum system, Phys. Rev. Lett. **117**, 240502 (2016).

[32] G. T. Landi and M. Paternostro, Irreversible entropy production: From classical to quantum, Rev. Mod. Phys. **93**, 035008 (2021).

[33] U. Seifert, Stochastic thermodynamics, fluctuation theorems and molecular machines, Rep. Prog. Phys. **75**, 126001 (2012).

[34] I. A. Martínez, E. Roldan, L. Dinis, D. Petrov, J. M. R. Parrondo, and R. A. Rica, Brownian Carnot engine, Nat. Phys. **12**, 67 (2016).

[35] M. N. Bera, A. Riera, M. Lewenstein, and A. Winter, Generalized laws of thermodynamics in the presence of correlations, Nat. Commun. **8**, 2180 (2017).

[36] A. F. Ducuara, C. E. Susa, and J. H. Reina, Emergence of maximal hidden quantum correlations and its trade-off with the filtering probability in dissipative two-qubit systems, Phys. A: Stat. Mech. App. **594**, 127035 (2022).

[37] F. Sapienza, F. Cerisola, and A. J. Roncaglia, Correlations as a resource in quantum thermodynamics, Nat. Commun. **10**, 2492 (2019).

[38] C. A. Melo-Luna, C. E. Susa, A. F. Ducuara, A. Barreiro, and J. H. Reina, Quantum locality in game strategy, Sci. Rep. **7**, 44730 (2017).

[39] K. Zawadzki, R. M. Serra, and I. D'Amico, Work-distribution quantumness and irreversibility when crossing a quantum phase transition in finite time, Phys. Rev. Res. **2**, 033167 (2020).

[40] C. I. Henao and R. M. Serra, Role of quantum coherence in the thermodynamics of energy transfer, Phys. Rev. E **97**, 062105 (2018).

[41] K. Micadei, J. P. S. Peterson, A. M. Souza, R. S. Sarthour, I. S. Oliveira, G. T. Landi, T. B. Batalhão, R. M. Serra, and E. Lutz, Reversing the direction of heat flow using quantum correlations, Nat. Commun. **10**, 2456 (2019).

[42] B. S. Revathy, V. Mukherjee, U. Divakaran, and A. del Campo, Universal finite-time thermodynamics of many-body quantum machines from Kibble-Zurek scaling, Phys. Rev. Res. **2**, 043247 (2020).

[43] B. P. Venkatesh, P. Talkner, M.-J. Hwang, and A. del Campo, Quantum statistical enhancement of the collective performance of multiple bosonic engines, Phys. Rev. Lett. **124**, 210603 (2020).

[44] V. Mukherjee and U. Divakaran, Many-body quantum thermal machines, J. Phys.: Condens. Matter **33**, 454001 (2021).

[45] M. Asadian, S. Ahadpour, and F. Mirmasoudi, Quantum correlated heat engine in XY chain with Dzyaloshinskii-Moriya interactions, Sci. Rep. **12**, 7081 (2022).

[46] A. de Oliveira Junior and M. C. de Oliveira, Unravelling the non-classicality role in Gaussian heat engines, Sci. Rep. **12**, 10412 (2022).

[47] P. A. Camati, J. F. G. Santos, and R. M. Serra, Coherence effects in the performance of the quantum Otto heat engine, Phys. Rev. A **99**, 062103 (2019).

[48] G. Francica, J. Goold, and F. Plastina, The role of coherence in the non-equilibrium thermodynamics of quantum systems, Phys. Rev. E **99**, 042105 (2019).

[49] J. P. Santos, L. C. Céleri, G. T. Landi, and M. Paternostro, The role of quantum coherence in non-equilibrium entropy production, npj Quantum Inf. **5**, 23 (2019).

[50] J. J. Alonso, E. Lutz, and A. Romito, Thermodynamics of weakly measured quantum systems, Phys. Rev. Lett. **116**, 080403 (2016).

[51] X. Ding, J. Yi, Y. W. Kim, and P. Talkner, Measurement driven single temperature engine, Phys. Rev. E **98**, 042122 (2018).

[52] L. Bresque, P. A. Camati, S. Rogers, K. Murch, A. N. Jordan, and A. Auff'eves, Two-qubit engine fueled by entanglement and local measurements, Phys. Rev. Lett. **126**, 120605 (2021).

[53] L. Buffoni, A. Solfanelli, P. Verrucchi, A. Cuccoli, and M. Campisi, Quantum measurement cooling, Phys. Rev. Lett. **122**, 070603 (2019).

[54] C. Elouard and A. N. Jordan, Efficient quantum measurement engines, Phys. Rev. Lett. **120**, 260601 (2018).

[55] M. F. Anka, T. R. de Oliveira, and D. Jonathan, Measurement-based quantum heat engine in a multilevel system, Phys. Rev. E **104**, 054128 (2021).

[56] V. F. Lisboa, P. R. Dieguez, J. R. Guimarães, J. F. G. Santos, and R. M. Serra, Experimental investigation of a quantum heat engine powered by generalized measurements, Phys. Rev. A **106**, 022436 (2022).

[57] G. Rubino, G. Manzano, and C. Brukner, Quantum superposition of thermodynamic evolutions with opposing time's arrows, Commun. Phys. **4**, 251 (2021).

[58] D. Felce and V. Vedral, Quantum refrigeration with indefinite causal order, Phys. Rev. Lett. **125**, 070603 (2020).

[59] H. Cao, N.-n. Wang, Z.-A. Jia, C. Zhang, Y. Guo, B.-H. Liu, Y.-F. Huang, C.-F. Li, and G.-C. Guo, Quantum simulation of indefinite causal order induced quantum refrigeration, Phys. Rev. Res. **4**, L032029 (2022).

[60] D. Felce, V. Vedral, and F. Tennie, Refrigeration with indefinite causal orders on a cloud quantum computer, arXiv:2107.12413.

[61] K. Simonov, G. Francica, G. Guarnieri, and M. Paternostro, Work extraction from coherently activated maps via quantum switch, Phys. Rev. A **105**, 032217 (2022).

[62] P. R. Dieguez, V. F. Lisboa, and R. M. Serra, Thermal devices powered by generalized measurements with indefinite causal order, Phys. Rev. A **107**, 012423 (2023).

[63] IBM Quantum. https://quantum-computing.ibm.com/ (2022).

[64] M. Campisi, J. Pekola and R. Fazio, Nonequilibrium fluctuations in quantum heat engines: Theory, example, and possible solid state experiments, New J. Phys. **17**, 035012 (2015).

[65] A. M. Timpanaro, G. Guarnieri, J. Goold, and G. T. Landi, Thermodynamic uncertainty relations from exchange fluctuation theorems, Phys. Rev. Lett. **123**, 090604 (2019).

[66] At this point, we note note that non-classical correlations could be provided in various ways, e.g., by cooling an interacting many-body fluid to its ground/low-energy state with related creation of (thermal) entanglement. This kind of non-classical correlations which are present in many-body thermal states could be used in further applications to obtain some quantum advantage in thermal protocols.

[67] H. Ollivier and W. H. Zurek, Quantum discord: A measure of the quantumness of correlations, Phys. Rev. Lett. **88**, 017901 (2001).

[68] QISKIT tomography. https://ignis.verification.tomography.

[69] B. Dakić, V. Vedral, and č. Brukner, Necessary and sufficient condition for nonzero quantum discord, Phys. Rev. Lett. **105**, 190502 (2010).

[70] D. Girolami, and G. Adesso, Observable measure of bipartite quantum correlations, Phys. Rev. Lett. **108**, 150403 (2012).